Magneto-thermoelectric effects in magnetic nanowire networks

22

Tristan da Câmara Santa Clara Gomes [1, 2], *Nicolas Marchal* [1], *Joaquín de la Torre Medina* [3], *Flavio Abreu Araujo* [1] and *Luc Piraux* [1]
[1]Institute of Condensed Matter and Nanosciences, Université catholique de Louvain, Louvain-la-Neuve, Belgium; [2]INESC Microsistemas e Nanotecnologias (INESC MN), Lisbon, Portugal; [3]Instituto de Investigaciones en Materiales/Unidad Morelia, Universidad Nacional Autónoma de México, Morelia, Mexico

22.1 Introduction

Recent advancements in three-dimensional (3D) networks made of interconnected nanowires (NWs) or nanotubes (NTs) have opened new possibilities in the field of thermoelectricity [1–8]. These nanoarchitectures offer several significant advantages over traditional parallel NW arrays. Notably, the 3D NW networks provide enhanced structural robustness and are well suited to electrical and thermoelectric measurements carried out in the plane of the film containing the NW arrays [5–8]. This enables the application of thermal and electrical currents in the macroscopic in-plane direction, while these currents remain locally restricted along the NW axes. Therefore, it allows for higher temperature gradients at the sample edges, thus enhancing the thermoelectric output signal compared to parallel NW arrays, where the application of currents is limited to the direction perpendicular to the film, with a thickness restricted to few tens of micrometers.

These 3D NW networks are embedded into polymer membranes, giving the NW–membrane composite flexibility while protecting the NWs from oxidation. As a result, 3D NW networks hold promise for flexible thermoelectricity devices [5,6,9]. Flexible thermoelectric materials and devices, capable of harnessing the thermal energy of hot surfaces with complex geometries or even that of the human body to convert heat into electricity, offer interesting opportunities for sustainable energy solutions [10–16]. These flexible thermoelectric generators are particularly well-suited to meet the growing demand for miniature, lightweight, and functional portable electronic devices, such as wearable sensors for medical applications [10,13].

Although the development of most flexible thermoelectric materials is based on the use of conventional thermoelectric materials [10–13], ferromagnetic metals also present promising prospects [17–19]. Indeed, ferromagnetic metals exhibit relatively large thermopowers, which can be attributed to the pronounced structure of the d-band and the high energy derivative of the density of states at the Fermi level [17]. Furthermore, magnon-drag contributions can add a significant contribution to the thermoelectric power over a broad temperature range [17,18,20–23]. These materials are particularly attractive for active Peltier cooling, which has gained attention as electronic

Magnetic Nano- and Microwires. https://doi.org/10.1016/B978-0-443-36534-8.00009-9

products—such as computer processors, LEDs, and batteries—demand more efficient and dynamic cooling solutions. Dynamic thermal management strategies are required to rapidly dissipate heat peaks that may disrupt device performance [24,25]. Active Peltier cooling has emerged as a viable option in this regard, allowing for precise temperature control and adaptability to rapid changing thermal conditions during operation, thus allowing to minimize hotspots and temperature spikes [26]. In this particular regime of active cooling [27–30], the Peltier heat flow generated by the electric current is added to the natural flow of heat from the hot to the cold side. In this case, materials must exhibit a high power factor (PF=$S^2\sigma$, with σ the electrical conductivity and S the Seebeck coefficient), and high thermal conductivity κ [27–30]. Among known materials, bulk cobalt emerges as an optimal choice for active cooling [28], offering the highest room-temperature (RT) thermoelectric power factor around 15 mW/K^{2}m [19].

In addition, the 3D magnetic network system has proven to be an ideal platform for exploiting spin-enabled transport mechanisms while maintaining a macroscopic and efficient thermoelectric output system. Notably, multilayer NW networks, consisting of alternating ferromagnetic and copper layers stacked along the NW axis, have proven to be effective and flexible materials for spin caloritronics [3,4,31]. Such innovative spin-based transport mechanisms are crucial steps in developing the next generation of thermoelectric materials [32]. The emerging field of spin caloritronics focuses on coupling heat-driven transport with spintronics, unlocking a range of novel transport phenomena [33,34]. Various spin-enabled mechanisms have been observed in nanoscale metal structures, magnetic tunnel junctions, and magnetic insulators [35–41]. However, the low conversion efficiency and limited power output of spin caloritronic devices have restricted their application as efficient heat harvesters [37,40–42]. In contrast, 3D magnetic multilayer NW networks allow for the efficient combination of the nanoscale lateral dimensions required for spin-enabled mechanisms with the macroscopic overall dimensions needed for large thermoelectric outputs and reliable measurements. In addition, the flexibility of the composite makes it particularly attractive for practical applications, as it allows for better adaptability to various form factors and environments.

In this chapter, we detail in Section 22.2, the fabrication techniques used to create flexible and robust films composed of interconnected and self-supporting nanowires, nanotubes and multilayers, whose size, geometry, composition, and morphology are controlled. Section 22.3 presents the thermoelectric properties of homogeneous arrays of ferromagnetic nanowires and nanotubes. Finally, in Section 22.4, we explore how nanowire arrays formed from magnetic multilayers can be used as flexible, macroscopic thermoelectric devices that exploit the spin degree of freedom. As an example, we discuss the realization and properties of magnetically activated thermoelectric switches.

22.2 Fabrication process and thermoelectric measurements of 3D interconnected magnetic nanowire and nanotube networks

Template-assisted electrodeposition has been proven to be well-suited for the fabrication of large-area 3D NW networks [43,44]. This method has been used to fabricate

large-area networks of homogeneous nanowires, nanotubes, and multilayer nanowires made of magnetic materials, arranged in 3D geometries [44–47]. The 3D magnetic NW and NT networks are obtained by direct electrodeposition into polycarbonate (PC) membranes with interconnected cylindrical nanochannels. The 22 μm-thick PC templates are created using a sequential multistep exposure to energetic heavy ions, at various angles with respect to the normal of the PC film surface [43,44]. The latent tracks are subsequently chemically etched, following a previously reported protocol, to obtain membranes with distinct porosities P and cylindrical pore diameters d [48]. In the present study, the templates are designed using four successive irradiation steps at angles of 25° (±5°) with respect to the out-of-plane direction of the membrane along two perpendicular directions within the plane of the membrane, as illustrated in Fig. 22.1A. The nanopore diameters are set within the range of 23–230 nm, while the porosity can vary from below 1% up to over 20%. More details regarding the geometries of the 3D nanopore networks are provided in Refs. [7,8]. The

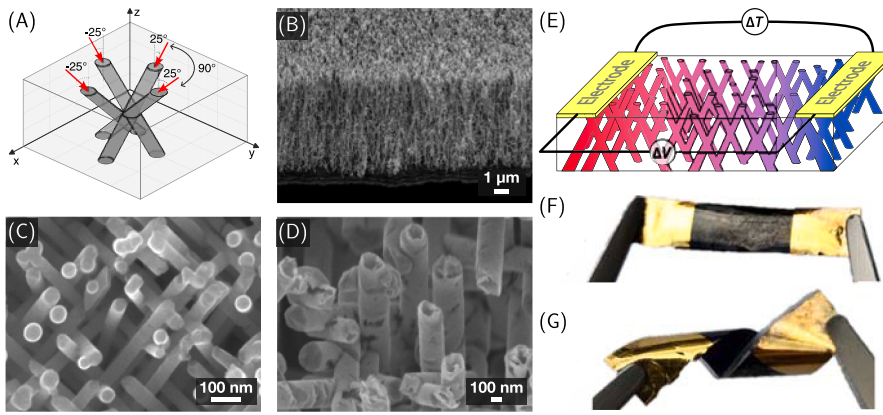

Figure 22.1 Three-dimensional interconnected networks and transport measurement configurations. (A) Schematic illustration of the four irradiation directions used in the track etching process, resulting in a 3D network of crossed nanopores. The irradiation directions are successively offset by 90° in the x-y plane, forming an angle of 25° with the z-axis. (B–D) scanning electron microscope (SEM) images of self-supported, mechanically stable networks composed of interconnected Ni nanowires and nanotubes. (B) Tilted view of a network film with a packing density of 20%. (C) SEM images of interconnected Ni nanowires with a diameter of 45 nm. (D) SEM images of interconnected Ni nanotubes with a diameter of 230 nm and a wall thickness of approximately 45 nm. (E) Schematic of the device configuration used for thermoelectric power measurements. A voltage difference ΔV arises due to heat flow generated by a temperature gradient ΔT between two metallic electrodes, measured by a thermocouple. The heat current flows overall in the x-direction, while being confined locally along the nanowire/nanotube axis. An external magnetic field can be applied in any direction within the y-z plane. (F–G) Photographs of the flexible nanocomposite device with two electrodes, illustrating its flexibility.
Adapted from Refs. [7,8,49].

complete filling of these templates by electrodeposition allows for achieving NW segment densities of up to 10^{13} segments per cm^2 of composite film.

3D magnetic NW networks made of homogenous pure ferromagnetic metal and alloys are fabricated via electrodeposition at RT using a simple potentiostatic mode [44–46]. The PC templates are first coated on one side with a metallic layer, which acts as the cathode during electrochemical deposition. A constant potential is applied between the cathode and a home-made electrolyte solution containing the desired metal ions, which are reduced and deposited within the nanopores. The alloy composition of the homogeneous NW networks can be precisely controlled by adjusting the composition of the electrolyte solution and/or the applied potential [23,46,50,51]. After electrodeposition, complete dissolution of the PC template results in a free-standing, interconnected metallic structure, as observed in the scanning electron microscope (SEM) images of a Ni NW network with 40 nm diameter nanowires, shown in Fig. 22.1B and C. The network replicates the complex branched morphology of the porous template. The degree of filling along the normal direction of the PC template can be controlled by adjusting the electrodeposition time.

Interconnected Ni NT networks are fabricated using an electrochemical dealloying method [47,52]. In the first reduction step, a Cu/Ni core–shell structure is grown within the PC template with a diameter of 230 nm. In the subsequent oxidation step, the Cu core is selectively removed, forming the hollow core of the Ni NTs. The NT wall thickness can be precisely tuned by adjusting the reduction potential, as demonstrated in Ref. [47]. In Fig. 22.1D, a SEM image of a Ni NT network after the complete removal of both the cathode and the PC template is presented, clearly illustrating the hollow core created by the full removal of the Cu core.

Additionally, 3D networks composed of multilayer NWs, where successive layers of ferromagnetic metals or alloys (FM) and copper (Cu) are stacked along the NW axes, can be grown using a pulsed electrodeposition technique within the host 3D porous templates [3,4,23,49,51]. The multilayer FM/Cu NWs are grown at RT via electrodeposition from a single electrolyte, using potentiostatic control and a pulsed electrodeposition technique [53]. This technique consists of alternating the deposition potential between a low potential, which deposits only Cu, and a higher potential, sufficient to deposit the FM layer, which contains a small percentage of Cu impurities. The concentration of Cu ions in the electrolyte solution is kept low to ensure that Cu contamination in the FM layer remained below 5%. Following a previously described procedure [54], the deposition rates of each metal are determined based on the pore filling time. The thickness of the bilayers, typically between 5 and 15 nm for both the FM and Cu layers, is optimized to achieve a strong giant magnetoresistance (GMR) effect.

The excellent electrical and thermal connectivity between the NWs enables easy transport measurements along the macroscopic in-plane direction, while the electrical and thermal currents are locally confined along the NW segments [3,45]. In all samples, the template is partially filled with either NWs, NTs, or FM/Cu NWs. For electrical and thermoelectric measurements, the metallic cathode is locally etched to create a multiprobe electrode pattern, as shown in Fig. 22.1E. A two-electrode design has been shown to be suitable for accurately measuring the resistance and Seebeck

coefficient of the various networks [3,5–8,45]. The measured areas typically measure 1–2 mm in length and 1 mm in width.

To measure the Seebeck coefficient, a temperature gradient is applied to the network by heating one electrode with a resistive heater, while the other electrode is maintained at a constant temperature. The voltage difference between the two electrodes is measured, while the temperature gradient is simultaneously recorded by a thermocouple. The contribution of the leads, made of calibrated Chromel P wires, is subtracted to obtain the Seebeck coefficient of the networks. Pictures of the magnetic network—PC template composite with the two electrodes, as well as the flexibility of the nanocomposite devices, are shown in Fig. 22.1F and G.

22.3 Thermoelectric properties of magnetic nanowire and nanotube networks

The thermopowers of homogeneous Fe, Co, Ni, and permalloy (Py, $Ni_{80}Fe_{20}$) NW networks with diameters d of 23 and 80 nm are reported for temperatures ranging from 100 to 300 K in Fig. 22.2. The figure also includes data for a Ni NT network with diameter d of 230 nm and a wall thickness t of approximately 45 nm. The results reveal almost no variation in thermopower with the dimensions for all the considered materials [7,8]. For Co NWs, the data in Fig. 22.2 also indicate that the thermopower is not affected by changes in crystalline structure. In addition, we observe a similar temperature dependence of the Seebeck coefficient in the Ni NT network compared to the Ni NW networks, suggesting that the complex nanostructure with its high surface-to-volume ratio does not significantly affect the relatively high Seebeck coefficient of Ni. The Seebeck coefficient values measured at RT for Fe, Co, Ni, and Py

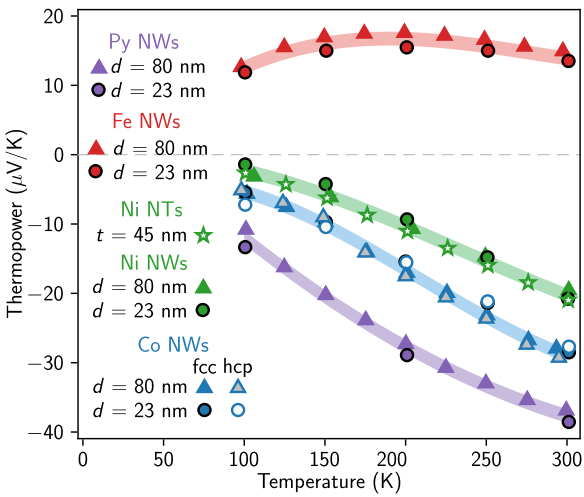

Figure 22.2 Evolution of the Seebeck coefficient as a function of temperature for interconnected ferromagnetic nanowires (NWs) with varying diameters d and interconnected Ni nanotubes (NTs) with a wall thickness t of 45 nm. Measurements are reported for Co nanowires with dominant face-centered cubic (fcc) and hexagonal close-packed (hcp) crystalline structures. Error bars, reflecting the uncertainty of the voltage and temperature measurements, are smaller than the symbol size.
Reprinted from Refs. [7,8]; with the permission of AIP Publishing.

NWs are very close to those of the bulk material, indicating that macroscopic interconnected networks of ferromagnetic nanofibers retain the good thermoelectric properties of their bulk counterparts, even with nanofiber diameters as small as 23 nm [7,8]. This makes them promising materials for thermoelectric applications [5,6]. Interestingly, both positive and negative thermopower can be achieved, enabling the fabrication of p–n thermoelectric junctions [5,6].

Figure 22.2 also reveals that, unlike the other ferromagnetic metals which display a negative thermopower dominated by the diffusion component with an almost linear temperature dependence, Fe NW networks exhibit a significantly large and positive Seebeck coefficient with a more complex temperature evolution. Recent work by Ref. [23] attributes this behavior to a pronounced magnon drag effect, which competes with the diffusion thermopower component, similar to what has been previously reported for bulk Fe [18,20–22]. The total thermopower of Fe NW networks can be expressed as

$$S = S_{\mathrm{d}} + S_{\mathrm{md}}, \tag{22.1}$$

where S_{d} and S_{md} are the diffusion and magnon-drag contributions to the thermopower, respectively. The two contributions are schematically illustrated in Fig. 22.3A. According to Mott' formula [17], the diffusion contribution to the thermopower can be approximated in its simplest form as $S_{\mathrm{d}} = \alpha T$, where α is the slope of the linear temperature dependence.

In Fig. 22.3B, the temperature dependence of the thermopower for NW networks made of pure Fe and $Fe_{100-x}Cu_x$ alloys, with $x = 2$, 7, 10, is shown for temperatures between 70 and 320 K.

For pure Fe NWs, the thermopower is positive for the whole temperature range considered, peaking at 16 μV/K around $T = 200$ K. These value are consistent with previous reports for bulk Fe [20,55]. The addition of Cu impurities in Fe leads to a decrease in thermopower, which becomes negative for the $Fe_{90}Cu_{10}$ NW network across most of the temperature range, reaching ~ −7 μV/K at 300 K. Furthermore, above $T \approx 200$ K, the $Fe_{100-x}Cu_x$ NWs exhibit a linear relationship between thermopower and temperature, with a slope $\alpha \approx -0.05$ μV/K^2. This slope value is similar to values derived from high-temperature measurements on bulk Fe [20], bulk diluted FeCo alloys [22], and bulk diluted FePt alloys [20]. The extracted slopes α for the FeCu NWs are reported in Fig. 22.3C, compared with bulk Fe and diluted FeCo and FePt alloys. All exhibit similar slopes of $\alpha \approx -0.05 \pm 0.01$ μV/K^2 (gray area in Fig. 22.3C). This analysis indicates that the diffusion thermopower is negative in Fe, as it is in Co and Ni [17,18,56,57].

Assuming the diffusion contribution to the thermopower in Fe NWs is given as $S_{\mathrm{d}} = -0.05T$ (dashed black line in Fig. 22.3D), it leads to a diffusion contribution to the thermopower of approximately −15 μV/K at $T = 300$ K. Therefore, the positive thermopower of Fe at RT results from a large and positive magnon-drag contribution to the thermopower. The magnon-drag contribution S_{md} can be extracted from Eq. (22.1) and is represented by purple dots in Fig. 22.3D, reaching approximately +30 μV/K at $T = 300$ K. As shown in Fig. 22.3B, the magnon-drag effect diminishes

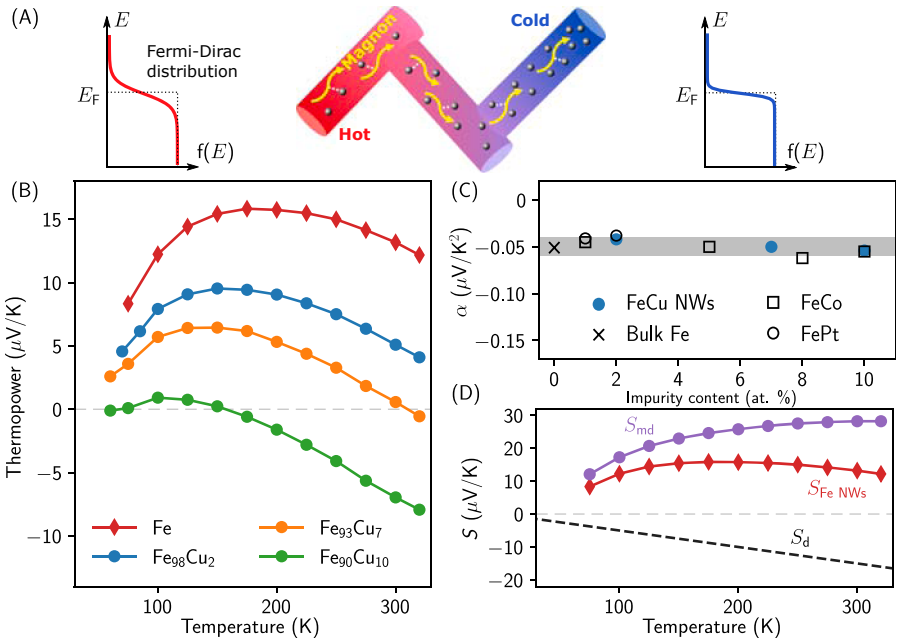

Figure 22.3 Thermopower of interconnected Fe-based nanowire networks. (A) Illustration of the diffusion thermopower caused by the difference in Fermi-Dirac distribution widths at the hot and cold ends of the sample, alongside a schematic of the magnon-drag effect in interconnected magnetic nanowires. (B) Temperature dependence of the thermopower S of nanowire networks made of pure Fe and Fe-rich FeCu alloys. (C) Estimated slope values a for the linear decay of $S(T)$ at temperatures $T > 200$ K for bulk Fe and dilute Fe-based alloys with impurity content below 10%. The shaded region highlights α values in the range of -0.05 ± 0.01 μV/K^2. (D) Seebeck coefficient of Fe nanowires, together with its estimated diffusion and magnon drag contributions, S_d and S_{md}, as derived from the analysis in Ref. [23]. Error bars in (B) and (C), reflecting the uncertainty of the voltage and temperature measurements, are smaller than the symbol size.
Adapted from Ref. [23].

progressively with the introduction of dilute Cu impurities, likely due to enhanced magnon-impurity scattering [23]. In contrast, the results in Fig. 22.2 indicate that this large and positive magnon-drag thermopower remains in Fe NW networks for lateral dimension down to 23 nm.

Marchal et al. [23] also reported a contrasting effect when diluted Cr impurities are added to Fe NW networks. The total Seebeck coefficient at RT initially increases slightly, then decreases, but remains around +10 μV/K for Cr impurities as high as 10%, as shown in Fig. 22.4A and B. Additionally, the linear decay near RT progressively vanishes as the Cr content increases (see Fig. 22.4A). This behavior is attributed to a reduction in the amplitude of the negative diffusion contribution caused by Cr impurities, which competes with the diminishing positive magnon-drag contribution. A similar reduction in the negative diffusion thermopower upon adding Cr impurities

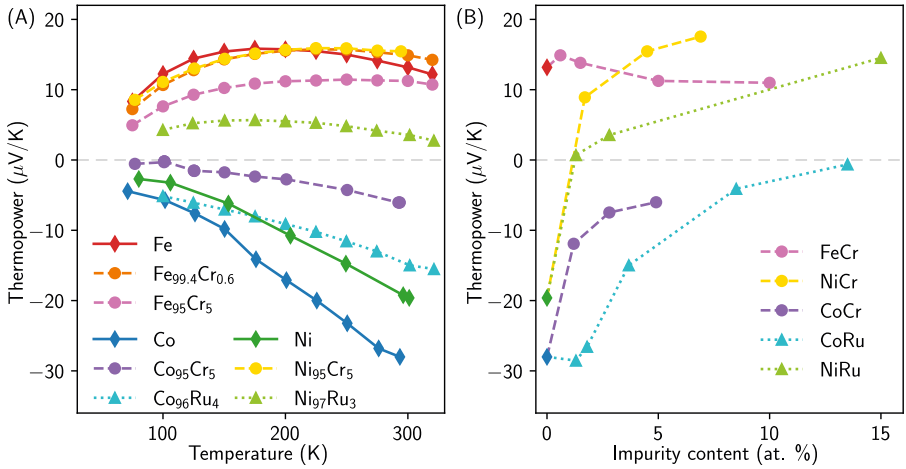

Figure 22.4 Thermoelectric characteristics of diluted Cr and Ru ferromagnetic alloy nanowires. (A) Temperature dependence of the Seebeck coefficient S for dilute FeCr, CoCr, NiCr, CoRu, and NiRu alloy nanowires compared to pure Fe, Co and Ni nanowires [23,50]. (B) Room temperature Seebeck coefficient as a function of impurity concentration for FeCr, CoCr, NiCr, CoRu, and NiRu nanowires. Error bars in (A and B), reflecting the uncertainty of the voltage and temperature measurements, are smaller than the symbol size.

has also been observed by Ref. [50] in diluted NiCr and CoCr NW networks. Fig. 22.4A compares the temperature evolution of the thermopower between 70 and 320 K for NW networks made of pure Fe, Co, and Ni with those of diluted FeCr, CoCr, and NiCr alloys, illustrating the observed trends. Notably, the addition of Cr impurities in Ni NWs alters the sign of the thermopower, with the Seebeck coefficient reaching +15.5 μV/K at RT for 5% of Cr into Ni NWs. Interestingly, recent measurements on diluted NiRu and CoRu show a similar effect, where the introduction of small amounts of Ru into Ni and Co NWs produces comparable changes, as depicted in Fig. 22.4A.

The RT evolution of the thermopower for diluted Co, Ni and Fe alloy NWs is presented in Fig. 22.4B. The results show that the introduction of Cr into Fe NWs does not significantly alter its positive thermopower. In contrast, the addition of Cr or Ru to Ni NWs results in a large, positive thermopower, enabling fine-tuning of the Seebeck coefficient by controlling the impurity concentration. For diluted Co alloys, the introduction of both Cr and Ru impurities progressively reduce the negative thermopower toward zero. As suggested in Ref. [50], these effects can be explained on the basis of a virtual bound state passing through the Fermi level in the spin up band [58,59]. Notably, similar changes in thermopower sign have also been reported in bulk NiCr alloys where minority spin dominates the electrical conduction [58–60].

Interestingly, these ferromagnetic NW networks combine high thermoelectric power factors PF, large Seebeck coefficients S of adjustable sign depending on the material, as well as high thermal conductivities κ [5,6,9]. This is illustrated in Table 22.1, which presents the RT values for the Seebeck coefficient, electrical resistivity, and power factor for several nanowire networks made of ferromagnetic metals and alloys.

Table 22.1 Room-temperature Seebeck coefficient S, resistivity p, and power factor PF for several nanowire networks made of ferromagnetic metals and alloys [5,6,23,50].

	S (μV/K)	ρ (μΩcm)	PF (mW/K^{2}m)		S (μV/K)	ρ (μΩcm)	PF (mW/K^{2}m)
Co	−28.0	7.1	11.0	$Ni_{95}Cr_5$	+15.5	27.3	0.9
Fe	+15.0	12.8	1.8	$Ni_{93}Cr_7$	+17.6	–	–
Ni	−19.6	9.1	4.2	$Ni_{85}Ru_{15}$	+14.5	–	–
$Ni_{90}Fe_{10}$	−34.4	18.6	6.3	$Co_{95}Cr_5$	−6.0	–	–
$Ni_{80}Fe_{20}$	−36.9	25.0	5.4	$Co_{99}Ru_1$	−28.5	–	–
$Ni_{70}Fe_{30}$	−40.2	32.5	5.0	$Fe_{99}Cr_1$	+14.9	–	–
$Ni_{60}Fe_{40}$	−46.0	42.4	5.0	$Fe_{95}Cr_5$	+11.3	–	–

Additionally, the room temperature figure of merit ($ZT = \mathrm{PF}/\kappa\, T$) for Co, Ni, and Fe NWs is found to be $3.2{\cdot}10^{-2}$, $1.6{\cdot}10^{-2}$, and $9.1{\cdot}10^{-3}$, respectively, while values up to $8.6{\cdot}10^{-2}$ were obtained for NiFe alloys [5,6,31]. Fig. 22.5A compares their performance to various flexible thermoelectric materials reported in the literature [10–12]. As suggested by the results in Fig. 22.5A, ferromagnetic NWs are promising candidates for active thermoelectric cooling applications, which require materials with both a high power factor and high thermal conductivity [27,28]. The schematics in Fig. 22.5B and C illustrate the difference between active thermoelectric cooling and conventional refrigeration. In active cooling (Fig. 22.5B), both Peltier flow and Fourier heat conduction move from the hot side to the cold side, whereas in refrigeration (Fig. 22.5C), these heat flows oppose each other. A demonstration of flexible active cooling devices using Co–Fe NW networks-based thermocouples has been recently presented by Ref. [9].

22.4 Magneto-thermoelectric properties of multilayer nanowire networks

This section focuses on the strong variation in thermopower found in crossed multilayer NW network films subjected to an external magnetic field. In these architectures, the overall thermal/electrical currents flow along the macroscopic in-plane direction of the film, while being locally restricted along the NW segments, as illustrated in Fig. 22.6A. This geometry enables the measurement of giant magnetoresistance (GMR) and magneto-thermopower responses with the current flowing perpendicularly to the plane of the layers in the individual NW segments (CPP configuration) while maintaining simple and reliable measurement along the macroscopic plane of the 3D network film [3,4,31,49,52]. GMR values up to 43% at $T = 300$ K and 86% at $T = 15$ K were found in $Co_{50}Ni_{50}$/Cu multilayer NWs [3,52].

In FM/Cu multilayer NW networks, the Seebeck coefficient along the axial direction (perpendicular direction to the layers) can be calculated using Kirchhoff's rules

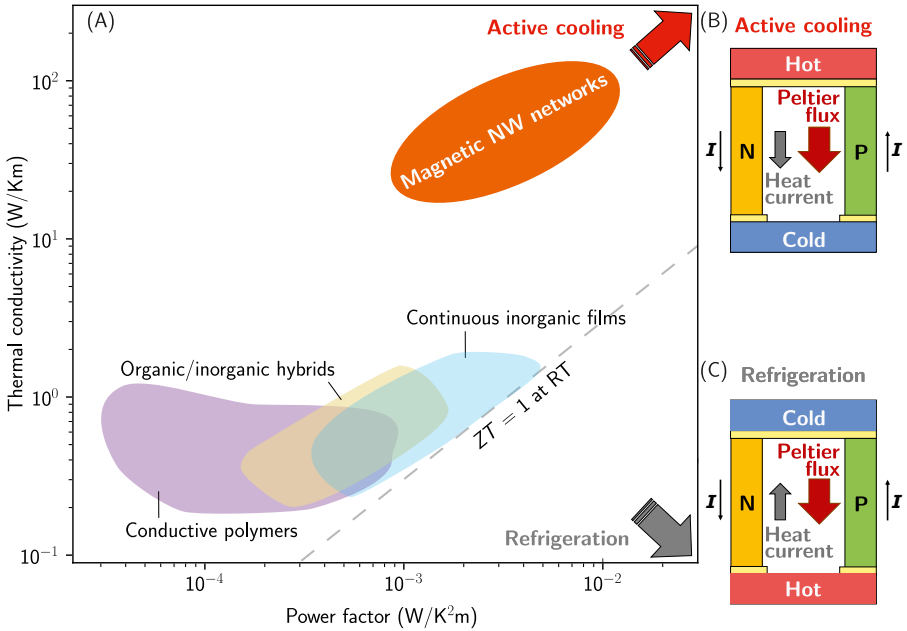

Figure 22.5 Comparison of active cooling performance among various flexible thermoelectric materials. (A) Thermoelectric power factor PF versus thermal conductivity κ for flexible thermoelectric systems made from magnetic nanowire networks [5,6,9], conductive polymers, organic/inorganic hybrids and continuous inorganic films [10–12]. The gray dashed line indicates the $ZT = 1$ case (where $Z = \mathrm{PF}/\kappa$, the figure of merit) which corresponds to the best power conversion efficiency achievable to date. The most suitable active Peltier coolers are positioned in the top right of the graph, as indicated by the red arrow. In contrast, the materials best suited for conventional Peltier refrigeration are located at the bottom right, as marked by the gray arrow. (B and C) schematic representations illustrating the differences between active cooling (B) and refrigeration (C). In the active cooling mode, Peltier heat flows from the hot side to the cold side, enhancing Fourier heat conduction, rather than opposing it as in the refrigeration mode.
Adapted from Ref. [9].

[61] as $S_\perp = (S_{Cu}\kappa_{FM} + \lambda S_{FM}\kappa_{Cu})/(\lambda\kappa_{Cu} + \kappa_{FM})$, where $S_{FM,\,Cu}$, and $k_{FM,\,Cu}$ are the thermopower and the thermal conductivity of the FM and Cu metals, respectively, and $\lambda = t_{FM}/t_{Cu}$ is the thickness ratio of FM and Cu layers. In metals, heat conductivity is predominantly driven by free electrons, and the Wiedemann-Franz law states that the ratio of thermal to electrical conductivity follows $\kappa/\sigma = LT$ where L is the Lorenz ratio. Therefore, for FM/Cu multilayers, this simplifies to

$$S_\perp = \frac{(S_{Cu}\rho_{Cu} + \lambda S_{FM}\rho_{FM})}{\lambda\rho_{FM} + \rho_{Cu}}, \tag{22.2}$$

with ρ_{FM} and ρ_{Cu} the corresponding electrical resistivities. According to this equation, $S_\perp$ is primarily influenced by the larger thermopower of the FM layer in case the

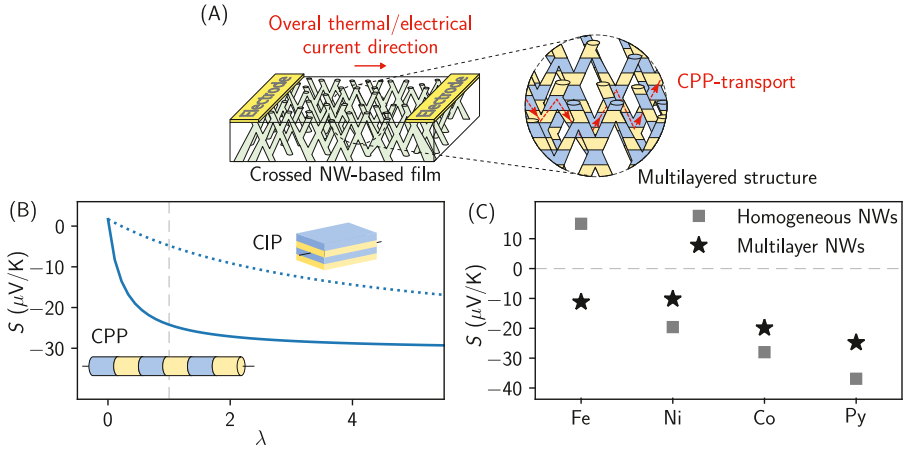

Figure 22.6 Thermopower in interconnected multilayer nanowire networks. (A) Schematic representation of the giant magnetoresistance and magneto-thermopower measurements in multilayer nanowire-based films, where the electrical/thermal transport takes place globally in the plane of the film while the architecture based on crossed nanowires ensures a current-perpendicular-to-plane (CPP) transport configuration. (B) Calculated thermopower for Co/Cu multilayers in both the current-in-plane (CIP, dotted line) and CPP (solid line) configurations as a function of the thickness ratio $\lambda = t_{Co}/t_{Cu}$, based on Eqs. (22.2) and (22.3) and the bulk values for S_{Co}, ρ_{Co}, S_{Cu}, and ρ_{Cu} [31]. (C) Comparison of the thermopower between FM/Cu nanowires and their corresponding homogeneous FM nanowires, where FM = Fe, Ni, Co, and Py. Error bars in (C), reflecting the uncertainty of the voltage and temperature measurements, are smaller than the symbol size.

thickness ratio λ is not too small, since $S_{FM}\rho_{FM} >> S_{Cu}\rho_{Cu}$. The same conclusion is drawn when the FM layer is formed from alloys such as CoNi and NiFe given the substantial difference in thermal conductivity between these alloys and Cu.

Conversely, the Seebeck coefficient for a planar FM/Cu multilayer in the direction parallel to the layers is expressed as

$$S_{\parallel} = \frac{(S_{Cu}\rho_{FM} + \lambda S_{FM}\rho_{Cu})}{\lambda\rho_{Cu} + \rho_{FM}}. \tag{22.3}$$

Here, a significant thermopower is only achievable when λ is very large. This contrast between the parallel and perpendicular directions is illustrated in Fig. 22.6B for Co/Cu multilayers, using bulk resistivity and thermopower values at room temperature. Therefore, these multilayer NW networks, composed of alternating ferromagnetic and noble metal stacks, hold promise as effective thermoelectric materials. Notably, thermopower values as high as $-32\,\mu V/K$ have been reported in $Ni_{60}Fe_{40}$/Cu multilayer NW networks [51].

In Fig. 22.6C, the RT thermopower of FM/Cu multilayer NW networks, where FM = Fe, Ni, Co, and Py ($Ni_{80}Fe_{20}$), is compared to that of their corresponding homogeneous FM NW networks. Only slight reductions in the absolute thermopower are

observed for Ni/Cu, Co/Cu and Py/Cu NWs when compared to Ni, Co, and Py NWs. However, for Fe/Cu NWs, a significant difference is observed, with a negative thermopower of approximately -11 μV/K measured at $T = 300$ K, contrasting with the large positive thermopower measured in homogeneous Fe NWs. This behavior can be attributed to negligible magnon–drag thermopower contribution in Fe/Cu NWs [23]. Assuming no magnon–drag contribution in Fe/Cu NWs, the measured thermopower of -11 μV/K -coincides well with the estimated diffusion contribution to the thermopower in Fe NWs, which is approximately -15 μV/K.

In Fig. 22.7AF, the magnetoresistance (in blue, left side) and magneto-thermoelectric (in red, right side) measurements at RT are displayed for various

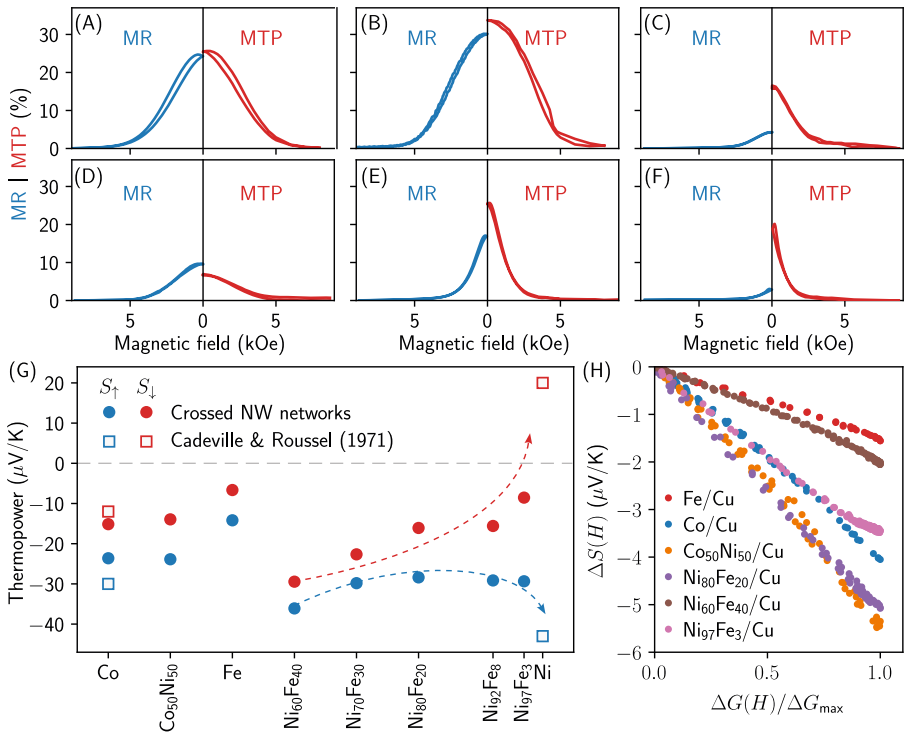

Figure 22.7 Room-temperature magneto-thermoelectric effect in multilayer nanowire networks. (A–F) Magnetoresistance (MR, left side, in blue) and magneto-thermopower (MTP, right side, in red) curves obtained by sweeping an external magnetic field along the in-plane direction of (A) Co/Cu [4], (B) $Co_{50}Ni_{50}$/Cu [3], (C) Fe/Cu [23], (D) $Ni_{60}Fe_{40}$/Cu, (E) $Ni_{80}Fe_{20}$/Cu, and (F) $Ni_{97}Fe_3$/Cu nanowire networks [51]. (G) calculated Seebeck coefficient for spin up ($S_\uparrow$, in *blue*) and spin down ($S_\downarrow$, in *red*) electrons using Eqs. (22.4) and (22.5) for various ferromagnetic metal (FM). Theoretical values from Ref. [59] are also included. (H) Linear variation of $\Delta S(H) = S(H) - S_0$ versus $\Delta G(H) = G(H) - G_0$, illustrating the Gorter-Nordheim characteristics for the multilayer FM/Cu nanowire networks shown in (A–F). For better visualization, $\Delta G(H)$ was normalized to its maximum value, ΔG_{max} to account for conductance differences in the FM/Cu samples. Error bars in (G), reflecting the uncertainty of the voltage and temperature measurements, are smaller than the symbol size.

FM/Cu NW networks, where FM = Co (A), $Co_{50}Ni_{50}$ (B), Fe (C), $Ni_{60}Fe_{40}$, (D), $Ni_{80}Fe_{20}$ (E), $Ni_{97}Fe_3$ (F). Here, MR(H)=($R(H)$ - R_{sat})/R_0, where $R(H)$ represents the resistance at a given external magnetic field value H, R_0, and R_{sat} are the resistances at $H = 0$ and at saturation field, respectively. Similarly, MTP(H) = |($S(H)$ - S_{sat})/S_0|, where $S(H)$ is the Seebeck coefficient at a given external magnetic field value H, S_0, and S_{sat} are the Seebeck coefficient at $H = 0$ and at saturation field, respectively. The absolute value of MTP is used to enable direct comparison between MR and MTP effects, as the negative Seebeck coefficient in these FM/Cu systems would otherwise result in a negative ($S(H)$ - S_{sat})/S_0 ratio.

In Fig. 22.7A and F, a similar magnetic variation behavior is observed for both resistance and thermopower across all samples, consistent with Mott's formula for diffusion thermopower. However, the results reveal that the amplitude of the MR and MTP can differ, particularly in Fe and NiFe alloys-based multilayers [23,51]. For Co/Cu and $Co_{50}Ni_{50}$/Cu, illustrated in Fig. 22.7A and B, notable MR and MTP effects are recorded with comparable amplitudes for both effects, reaching up to MR = 30% and MTP = 34% at RT for $Co_{50}Ni_{50}$/Cu NWs. In contrast, Fe/Cu NWs exhibit an MTP effect approximately four times greater than the corresponding MR effect [23]. Note that a similar trend is seen in Ni/Cu NWs, where the MTP effect is about four to five times larger than the corresponding MR effect at RT [31]. Interestingly, the NiFe alloys display contrasting relationships between the amplitudes of MR and MTP effects as the alloy composition varies. However, for $Ni_{60}Fe_{40}$/Cu and $Ni_{97}Fe_3$/Cu NWs, the MTP effect surpasses the MR effect, with the MTP effect in $Ni_{97}Fe_3$/Cu NWs being about seven times larger than the corresponding MR effect.

In the limits of no-spin relaxation, most of the CPP-GMR data can be understood using a simple two-current series-resistor model. In this model, the resistances of layers and interfaces simply add up, and "up" and "down" charge carriers propagate independently in two spin channels with large spin asymmetries of the electron's scattering [62,63]. Similarly, the Seebeck coefficients for spin-up ($S_\uparrow$) and spin-down ($S_\downarrow$) electrons are expected to differ significantly due to the exchange-split d-band structure in these ferromagnets, as suggested from previous studies performed on dilute magnetic alloys [58,59]. Assuming that the layers of the magnetic multilayers are thin relative to the spin-diffusion lengths, and applying the usual rule for current splitting between two parallel paths, it has been demonstrated that the spin-dependent Seebeck coefficients, $S_\uparrow$ and $S_\downarrow$, can be directly extracted from experimental data on FM/Cu NW networks as follows [3,4]:

$$S_\uparrow = \frac{1}{2}\left[S_0\left(1 - \mathrm{MR}^{-1/2}\right) + S_{sat}\left(1 + \mathrm{MR}^{-1/2}\right)\right] \tag{22.4}$$

and

$$S_\downarrow = \frac{1}{2}\left[S_0\left(1 + \mathrm{MR}^{-1/2}\right) + S_{sat}\left(1 - \mathrm{MR}^{-1/2}\right)\right], \tag{22.5}$$

where MR denotes the amplitude of the magnetoresistance effect (i.e., maximum values of MR(H) in Fig. 22.7AF).

In Fig. 22.7G, the values for $S_\uparrow$ and $S_\downarrow$ for various FM materials at RT are reported, calculated using Eqs. (22.4) and (22.5) with the measured value for the MR ratio, S_0 and S_{sat} for the FM/Cu NW networks [3,4,23,31,49,51]. For comparison, the values for $S_\uparrow$ and $S_\downarrow$ reported by Ref. [59] for bulk Co and Ni, extracted from diluted Ni-based and Co-based bulk alloys, are also shown in Fig. 22.7G. The spin-dependent Seebeck coefficients derived from the Co/Cu NW network align well with those of bulk Co. Fig. 22.7G also depicts the evolution of $S_\uparrow$ and $S_\downarrow$ for Ni_xFe_{1-x}/Cu NW networks, revealing an increasing gap between $S_\uparrow$ and $S_\downarrow$ as the Ni content rises toward 100%.

Specifically, the difference $(S_\uparrow - S_\downarrow)$ increases from approximately -7 μV/K for the $Ni_{60}Fe_{40}$/Cu sample to about -21 μV/K for the $Ni_{97}Fe_3$/Cu sample. This trend is consistent with previous work on diluted Ni-based alloys by Ref. [59]; which reported a very high ΔS value of about -60 μV/K for pure Ni. Note however that this ΔS value was not obtained for Ni/Cu NWs [31].

In Fig. 22.7H, the linear relationship at RT between the variation of thermopower $\Delta S(H) = (S(H) - S_0)$ and the variation of conductance $\Delta G(H) = (G(H) - G_0)$, where $G(H) = 1/R(H)$ and $G_0 = 1/R_0$, is reported for various FM/Cu NW networks. To improve visualization, the conductance variation for each sample was normalized to its maximum value, ΔG_{max}, due to the variation in resistance across the FM/Cu samples. These linear relationships provide evidence that thermopower in these FM/Cu multilayer NW networks is dominated by electron diffusion [3,4,31,49,51], including in the case of the Fe/Cu sample [23]. These curves correspond to Gorter–Nordheim plots for the diffusion thermopower in metals and alloys [17]. For magnetic multilayers, the Gorter–Nordheim relation can be expressed as [3,64].

$$S(H) = A + \frac{B}{R(H)}, \tag{22.6}$$

where $A = (S_0R_0 - S_{sat}R_{sat})/(R_0 - R_{sat})$ and $B = R_0R_{sat}(S_{sat} - S_0)/(R_0 - R_{sat})$.

Fig. 22.7H also provides the amplitudes of the magnetic-field induced variation in thermopower for FM/Cu NW networks. The $Co_{50}Ni_{50}$/Cu and Py/Cu samples exhibit the largest ΔS amplitudes, reaching -5.5 μV/K and -5.1 μV/K, respectively. These significant magnetic modulations of thermopower have been used by Refs. [5,6] to develop flexible thermoelectric switches triggered by magnetic field, using NW network-based thermocouples. A schematic of the thermocouple design is presented in Fig. 22.8A. The first branch of the thermocouple consists of an FM/Cu NW network (FM = $Co_{50}Ni_{50}$ or Py), which exhibits a large magnetic variation of its Seebeck coefficient. The second branch is made of homogeneous FM NWs, which show negligible magneto-transport effects (i.e., its thermopower is almost unchanged under the application of a magnetic field) [31]. The measured voltage generated by the NW-based thermocouple at RT due to a temperature gradient ΔT under an applied magnetic field H is given by

$$\Delta V(H) = \int_{T_0}^{T_0+\Delta T} \Big(S_{FM}(T) - S_{FM/Cu}(T,H)\Big)\,dT, \tag{22.7}$$

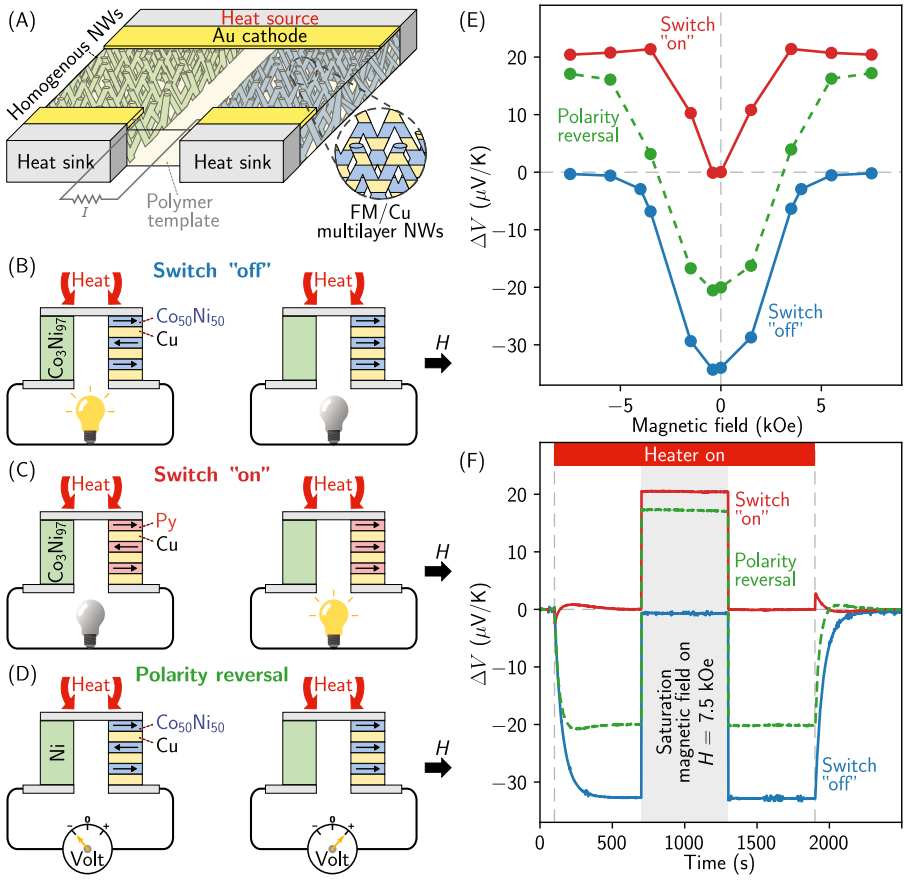

Figure 22.8 Demonstration of magnetically activated thermoelectric switches based on 3D magnetic nanowire network thermocouples. (A) Schematic of a magnetically activated thermoelectric switch thermocouple, where the two crossed nanowire network legs consist respectively of a homogeneous structure and an FM/Cu multilayer structure with giant magneto-Seebeck effect (FM = Py or $Co_{50}Ni_{50}$). The thermoelectric voltage generated by the heat flux between the heat source and the heat sinks (maintained at desired temperature via a PID temperature controller) can be switched off or on by applying an external magnetic field that saturates the successive magnetization of the multilayer structure. (B–D) schematics showing (B) a switch "off" device made of a $Ni_{50}Co_{50}$/Cu - Co_3Ni_{97} thermocouple, (C) a switch "on" device made of Py/Cu - Co_3Ni_{97} thermocouple and (D) a polarity reversal device made of a $Ni_{50}Co_{50}$/Cu–Ni thermocouple. (E) variation in the voltage differential ΔV recorded at the junction edges for a temperature gradient $\Delta T = 10$ K when sweeping a magnetic field from +7.5 kOe to −7.5 kOe in the plane of the switch "on" (in *red*), polarity reversal (in *green*) and switch "off" (in *blue*) nanowire network thermocouples at room temperature. (F) Time dependence of the thermoelectric voltage ΔV for the switch "on" (in *red*), polarity reversal (in *green*) and switch "off" (in *blue*) thermocouples. The heater is switched on after 100 s to create a temperature gradient $\Delta T = 10$ K. The *gray* area indicates the presence of an external magnetic field of 7.5 kOe. Error bars in (E), reflecting the uncertainty of the voltage and temperature measurements, are smaller than the symbol size. Adapted from Refs. [5,6]

where T_0 is the heat-sink base temperature, and S_{FM} and $S_{FM/Cu}(H)$ are the Seebeck coefficients of the homogeneous FM NWs and multilayer FM/Cu NWs, respectively. The entire device is embedded in a single flexible PC template, ensuring robustness and flexibility for practical applications.

By appropriately selecting the materials used in the FM/Cu and homogeneous FM NW networks, different switches can be achieved, as schematically represented in Fig. 22.8BD. For instance, the switch "off" device, which transitions from an "on state" (producing a measurable voltage of a few tens of μV) at zero magnetic field to an "off state" ($\Delta V = 0$) at the saturation magnetic field, is realized by a thermocouple made of $Co_{50}Ni_{50}$/Cu and Co_3Ni_{97} NW legs (see Fig. 22.8B). In contrast, a switch "on" device transitions from the "off state" at zero magnetic field to an "on state" at the saturation magnetic field (see Fig. 22.8C) and can be realized by a thermocouple composed of Py/Cu NWs and Co_3Ni_{97} NWs. Indeed, the RT thermopower of Co_3Ni_{97} NW networks aligns with both the saturated thermopower of $Co_{50}Ni_{50}$/Cu NWs and the zero-field thermopower of Py/Cu NWs (~ −21 μV/K) [5,6]. Additionally, this design can be used to achieve control of the thermoelectric voltage polarity (see Fig. 22.8D). In this case, magnetic saturation of the multilayer system leads to a polarity reversal in the thermoelectric voltage. Such a device can be realized by selecting $Co_{50}Ni_{50}$/Cu and Ni NWs as the thermoelements in the thermocouple.

In Fig. 22.8E, the voltage differential recorded at the edge of the switch "off" (in blue), switch "on" (in red) and polarity reversal (in green) devices is plotted as a function of the external magnetic field, for a temperature gradient $\Delta T = 10$ K applied to the devices, and heat sink maintained at RT. As shown, the switch "off" device enables the transition from approximately $\Delta V \approx -34$ μV at $H = 0$ to $\Delta V = 0$ at $H = 7.5$ kOe. Conversely, the switch "on" device transitions from $\Delta V = 0$ at $H = 0$ to $\Delta V \approx 21$ μV at $H = 7.5$ kOe. For the polarity reversal device, the thermoelectric voltage can be controlled in a range between −20 μV (at zero field) and +18 μV (at $H = 7.5$ kOe).

The time traces of thermoelectric voltage ΔV, shown in Fig. 22.8F, demonstrate the dynamic response of the thermoelectric switches. For each device, after 100 s, the heater is activated to apply a temperature differential of $\Delta T = 10$ K, establishing the zero-field voltage differential at the edges of the devices. Then, after 700 s, a magnetic field of $H = 7.5$ kOe is applied, leading to a change in the thermocouple output voltage. For the switch "off" device, this change results in the complete cancellation of the thermoelectric voltage. In contrast, the switch "on" device shows an increase in ΔV when the field is applied. For the polarity reversal device, the sign of the thermoelectric voltage is reversed. Once the magnetic field is removed, the thermoelectric voltage ΔV returns to its original state. Notably, the fully realized transition between the zero-field and saturation-field states occurs over a very short time interval, limited only by the rise time of the magnetic field.

These devices are robust, capable of repeatedly switching their thermoelectric output voltage on demand without degradation over multiple cycles of magnetic field changes and without cycles-induced deviation of the thermoelectric outputs at zero and saturation field [5,6]. Additionally, the voltage levels produced by these thermocouples are easily measurable and their use in TTL or CMOS logic circuits is rather

straightforward. Two degrees of freedom can be leveraged to enhance the output voltage of these devices: assembling multiple junctions in series and/or amplifying the resulting signal to the required logic voltage levels. This flexibility opens up opportunities for developing scalable thermoelectric devices that can be directly interfaced with modern electronic systems.

22.5 Conclusions

Macroscopic networks composed of interconnected ferromagnetic nanowire or nanotube embedded within flexible polymer films make unique composite structure that combine advantageous mechanical, magnetic, and thermoelectric properties. These features make them promising materials for efficient thermoelectric and spin caloritronic applications. The interconnected nanowire networks are robust and self-supported because they are grown as a single material through template-assisted electrodeposition, in contrast to disperse nanowire networks. Additionally, the polymer template embedding the network provides flexibility and shapeability, making these composites suitable for flexible magneto-electric and thermoelectric applications. This approach allows for the production of lightweight nanocomposite films featuring microscopic film thickness and macroscopic lateral dimensions without any lateral size limitations. The fabrication technique enables the creation of networks made of homogeneous nanowires with controlled alloy composition, nanotubes, as well as multilayer nanowires with sequenced material composition variations along the nanowire axes. Additionally, various geometrical parameters can be controlled, including the nanowire diameter, the network packing density (ranging from less than 1% up to over 20%), and filling along the normal direction of the polymer template. Notably, this technique allows to achieve nanowire segment densities up to 10^{13} segments per cm^2 in the composite film.

These NW networks provide an ideal structure to reliably measure thermoelectric and magneto-transport properties in their macroscopic in-plane directions, with transport locally restricted along the nanowire segments. Nanowire and nanotube networks made of ferromagnetic metals exhibit significant thermopower, comparable to that of their bulk constituents, even with diameters as small as 23 nm. Additionally, both negative and positive thermopower values are obtained, enabling the fabrication of p-n thermoelectric junctions made of interconnected ferromagnetic metal nanowires. While ferromagnetic metal nanowire networks, such as Ni or Co, tend to exhibit negative thermopower, positive thermopower is observed in Fe nanowires due to a significant and positive magnon–drag contribution that overcomes the large negative diffusion thermopower contribution. Moreover, positive thermopower can also be achieved by introducing impurities like Ru and Cr within Ni nanowires. The high electronic conductivity and large thermopower of these 3D ferromagnetic nanowire networks results in significant power factor compared to other flexible thermoelectric materials, along with high thermal conductivity, making them ideal candidates for active thermoelectric cooling applications.

These remarkable thermoelectric properties are preserved in 3D multilayer nanowire networks, where ferromagnetic metal and copper layers are successively stacked

along the nanowire axis. These original nanoarchitectures using CNWs exhibit giant magneto-resistance and giant magneto-thermoelectric effects, with heat and electrical currents flowing perpendicular to the successive layers in a current-perpendicular-to-plane configuration. In this arrangement, the thermopower of multilayer nanowires is found to be close to that of homogeneous nanowires made of identical ferromagnetic metals, achieving thermopower values of up to -32 μV/K in $Ni_{60}Fe_{40}$/Cu nanowires. In the case of Fe/Cu nanowires, the multilayer structure suppresses the positive magnon-drag contribution, resulting to negative thermopower close to that of the diffusion contribution in Fe nanowires. These thermopower can be highly modulated by a magnetic field, with absolute variations reaching -5.5 μV/K and -5.1 μV/K in $Co_{50}Ni_{50}$/Cu and Py/Cu nanowires, respectively.

These giant magneto-thermoelectric effects arise from the different thermopower of spin up and spin down electrons in ferromagnetic metals. Interestingly, interconnected multilayer nanowire networks offer a platform to directly extract spin-dependent Seebeck coefficients, $S_\uparrow$ and $S_\downarrow$, from experimental measurements. The value obtained coincides well with previous values derived from bulk diluted alloys studies. Furthermore, $Ni_{100-x}Fe_x$/Cu nanowire networks display large $S_\uparrow - S_\downarrow$ difference as the Fe content is reduced to very low values. Finally, these networks can be used to create thermoelectric magnetic switches, formed from thermocouple films with legs made of homogeneous and multilayer nanowire networks. The thermoelectric voltage can switch between zero and a few tens of microvolts when the external magnetic field is turned on or off, showing potential applications in logic computing and sensors powered by waste heat.

In summary, this chapter highlights the potential for controlled template-assisted synthesis of complex nanowire-based architectures with excellent control over geometrical features, morphology, and chemical composition. This leads to tunable thermoelectric and magneto-thermoelectric properties, paving the way for advanced materials in energy conversion and electronic applications.

Acknowledgments

Financial support was provided by the Belgian Fund for Scientific Research (FNRS) and by the European Union. Views and opinions expressed are however those of the authors only and do not necessarily reflect those of the European Union or the European Research Executive Agency (REA). Neither the European Union nor the granting authority can be held responsible for them. T.d.C.S.C.G. is an ERA fellow. F.A.A. is a Research Associate of the F.R.S.-FNRS. J. d. l. T. M. thanks the 2025 UNAM-DGAPA-PAPIIT program for the financial support of project IN106025. The authors thank Dr. E. Ferain and the it4ip Company for supplying polycarbonate membranes.

References

[1] M.F.P. Wagner, A.S. Paulus, J. Brötz, W. Sigle, C. Trautmann, K.-O. Voss, F. Volklein, M.E. Toimil- Molares, Effects of size reduction on the electrical transport properties of 3D Bi nanowire networks, Adv. Electron. Mater. 7 (3) (2021) 2001069.

[2] L. Piraux, N. Marchal, P. Van Velthem, T. da Câmara Santa Clara Gomes, E. Ferain, J.-P. Issi, V.-A. Antohe, Polycrystalline bismuth nanowire networks for flexible longitudinal and transverse thermoelectrics, Nanoscale 15 (2023) 13708–13717.
[3] T. da Câmara Santa Clara Gomes, F. Abreu Araujo, L. Piraux, Making flexible spin caloritronic devices with interconnected nanowire networks, Sci. Adv. 5 (3) (2019a) eaav2782.
[4] F. Abreu Araujo, T. da Câmara Santa Clara Gomes, L. Piraux, Magnetic control of flexible thermo electric devices based on macroscopic 3d interconnected nanowire networks, Adv. Electron. Mater. 5 (8) (2019) 1800819.
[5] T. da Câmara Santa Clara Gomes, N. Marchal, F.A. Araujo, L. Piraux, Flexible thermoelectric films based on interconnected magnetic nanowire networks, J. Phys. Appl. Phys. 55 (22) (2022a) 223001.
[6] T. da Câmara Santa Clara Gomes, N. Marchal, F. Abreu Araujo, L. Piraux, Magnetically activated flexible thermoelectric switches based on interconnected nanowire networks, Adv. Mater. Technol. 7 (5) (2022b) 2101043.
[7] T. da Câmara Santa Clara Gomes, N. Marchal, A. Moureaux, S. de Wergifosse, C. Chopin, L. Piraux, J. de la Torre Medina, F. Abreu Araujo, Geometrical properties of three-dimensional crossed nanowire networks, Phys. Rev. Res. 6 (2024a) 023211.
[8] T. da Câmara Santa Clara Gomes, N. Marchal, J. de la Torre Medina, F. Abreu Araujo, L. Piraux, Thermoelectric and magneto-transport characteristics of interconnected networks of ferromagnetic nanowires and nanotubes, Appl. Phys. Lett. 124 (9) (2024b) 092406.
[9] T. da Câmara Santa Clara Gomes, N. Marchal, F. Abreu Araujo, L. Piraux, Flexible active peltier coolers based on interconnected magnetic nanowire networks, Nanomaterials 13 (11) (2023).
[10] Y. Wang, L. Yang, X.-L. Shi, X. Shi, L. Chen, M.S. Dargusch, J. Zou, Z.-G. Chen, Flexible thermoelectric materials and generators: challenges and innovations, Adv. Mater. 31 (29) (2019) 1807916.
[11] Z. Fan, Y. Zhang, L. Pan, J. Ouyang, Q. Zhang, Recent developments in flexible thermoelectrics: from materials to devices, Renew. Sustain. Energy Rev. 137 (2021) 110448.
[12] L. Zhang, X.-L. Shi, Y.-L. Yang, Z.-G. Chen, Flexible thermoelectric materials and devices: from materials to applications, Mater. Today 46 (2021) 62–108.
[13] T. Cao, X.-L. Shi, Z.-G. Chen, Advances in the design and assembly of flexible thermoelectric device, Prog. Mater. Sci. 131 (2023) 101003.
[14] J.-H. Bahk, H. Fang, K. Yazawa, A. Shakouri, Flexible thermoelectric materials and device optimization for wearable energy harvesting, J. Mater. Chem. C 3 (2015) 10362–10374.
[15] Y. Du, J. Xu, B. Paul, P. Eklund, Flexible thermoelectric materials and devices, Appl. Mater. Today 12 (2018) 366–388.
[16] S. Masoumi, S. O'Shaughnessy, A. Pakdel, Organic-based flexible thermoelectric generators: from materials to devices, Nano Energy 92 (2022) 106774.
[17] F.J. Blatt, P.A. Schroeder, C.L. Foiles, D. Greig, Thermoelectric Power of Metals, Springer, Boston, MA, 1976.
[18] S.J. Watzman, R.A. Duine, Y. Tserkovnyak, S.R. Boona, H. Jin, A. Prakash, Y. Zheng, J. P. Heremans, Magnon-drag thermopower and nernst coefficient in fe, co, and ni, Phys. Rev. B 94 (2016) 144407.
[19] K. Vandaele, S.J. Watzman, B. Flebus, A. Prakash, Y. Zheng, S.R. Boona, J.P. Heremans, Thermal spin transport and energy conversion, Mater. Today Phys. 1 (2017) 39–49.

[20] F.J. Blatt, D.J. Flood, V. Rowe, P.A. Schroeder, J.E. Cox, Magnon-drag thermopower in iron, Phys. Rev. Lett. 18 (1967) 395–396.
[21] A.D. Avery, R. Sultan, D. Bassett, D. Wei, B.L. Zink, Thermopower and resistivity in ferromagnetic thin films near room temperature, Phys. Rev. B 83 (2011) 100401.
[22] Y. Zheng, E.J. Weiss, N. Antolin, W. Windl, J.P. Heremans, Magnon drag effect in Fe-Co alloys, J. Appl. Phys. 126 (12) (2019) 125107.
[23] N. Marchal, T. da Câmara Santa Clara Gomes, F. Abreu Araujo, L. Piraux, Interplay between diffusion and magnon-drag thermopower in pure iron and dilute iron alloy nanowire networks, Sci. Rep. 13 (1) (2023) 9280.
[24] E. Pop, S. Sinha, K. Goodson, Heat generation and transport in nanometer-scale transistors, Proc. IEEE 94 (8) (2006) 1587–1601.
[25] Y. Cai, Y. Wang, D. Liu, F.-Y. Zhao, Thermoelectric cooling technology applied in the field of electronic devices: updated review on the parametric investigations and model developments, Appl. Therm. Eng. 148 (2019) 238–255.
[26] J. Sharp, J. Bierschenk, H. Lyon, Overview of solid-state thermoelectric refrigerators and possible applications to on-chip thermal management, Proc. IEEE 94 (8) (2006) 1602–1612.
[27] M. Zebarjadi, Electronic cooling using thermoelectric devices, Appl. Phys. Lett. 106 (20) (2015) 203506.
[28] M. Adams, M. Verosky, M. Zebarjadi, J. Heremans, Active Peltier coolers based on correlated and magnon-drag metals, Phys. Rev. Appl. 11 (2019) 054008.
[29] M. Parker, Going with the flow (of heat), Nat. Electron. 2 (6) (2019).
[30] J. Mao, G. Chen, Z. Ren, Thermoelectric cooling materials, Nat. Mater. 20 (4) (2021) 454–461.
[31] T. da Câmara Santa Clara Gomes, N. Marchal, F. Abreu Araujo, L. Piraux, Spin caloritronics in 3D interconnected nanowire networks, Nanomaterials 10 (2020) 2092.
[32] J. He, T.M. Tritt, Advances in thermoelectric materials research: looking back and moving forward, Science 357 (6358) (2017).
[33] G.E.W. Bauer, E. Saitoh, B.J. van Wees, Spin caloritronics, Nat. Mater. 11 (2012) 391.
[34] S.R. Boona, R.C. Myers, J.P. Heremans, Spin caloritronics, Energy Environ. Sci. 7 (2014) 885–910.
[35] K. Uchida, J. Xiao, H. Adachi, J. Ohe, S. Takahashi, J. Ieda, T. Ota, Y. Kajiwara, H. Umezawa, H. Kawai, G.E.W. Bauer, S. Maekawa, E. Saitoh, Spin seebeck insulator, Nat. Mater. 9 (2010) 894.
[36] C.M. Jaworski, J. Yang, S. Mack, D.D. Awschalom, J.P. Heremans, R.C. Myers, Observation of the spin-seebeck effect in a ferromagnetic semiconductor, Nat. Mater. 9 (2010) 898.
[37] A. Slachter, F.L. Bakker, J.-P. Adam, B.J. van Wees, Thermally driven spin injection from a ferromagnet into a non-magnetic metal, Nat. Phys. 6 (2010) 879.
[38] M. Hatami, G.E.W. Bauer, Q. Zhang, P.J. Kelly, Thermal spin-transfer torque in magnetoelectronic devices, Phys. Rev. Lett. 99 (2007) 066603.
[39] A. Pushp, T. Phung, C. Rettner, B.P. Hughes, S.-H. Yang, S.S.P. Parkin, Giant thermal spin-torque-assisted magnetic tunnel junction switching, Proc. Natl. Acad. Sci. 112 (21) (2015) 6585–6590.
[40] N. Liebing, S. Serrano-Guisan, K. Rott, G. Reiss, J. Langer, B. Ocker, H.W. Schumacher, Tunneling magnetothermopower in magnetic tunnel junction nanopillars, Phys. Rev. Lett. 107 (2011) 177201.
[41] M. Walter, J. Walowski, V. Zbarsky, M. Munzenberg, M. Schäfers, D. Ebke, G. Reiss, A. Thomas, P. Peretzki, M. Seibt, J.S. Moodera, M. Czerner, M. Bachmann, C. Heiliger, Seebeck effect in magnetic tunnel junctions, Nat. Mater. 10 (2011) 742.

[42] F.K. Dejene, J. Flipse, B.J. van Wees, Spin-dependent seebeck coefficients of ni8_0fe$_2$o and co in nanopillar spin valves, Phys. Rev. B 86 (2012) 024436.
[43] M. Rauber, I. Alber, S. Muller, R. Neumann, O. Picht, C. Roth, A. Schökel, M.E. Toimil-Molares, W. En- singer, Highly-ordered supportless three-dimensional nanowire networks with tunable complexity and interwire connectivity for device integration, Nano Lett. 11 (6) (2011) 2304–2310.
[44] E. Araujo, A. Encinas, Y. Velázquez-Galván, J.M. Martinez-Huerta, G. Hamoir, E. Ferain, L. Piraux, Artificially modified magnetic anisotropy in interconnected nanowire networks, Nanoscale 7 (2015) 1485–1490.
[45] T. da Câmara Santa Clara Gomes, J. de la Torre Medina, Y.G. Velázquez-Galván, J. M. Martinez-Huerta, A. Encinas, L. Piraux, Interplay between the magnetic and magneto-transport properties of 3d interconnected nanowire networks, J. Appl. Phys. 120 (4) (2016b) 043904.
[46] T. da Câmara Santa Clara Gomes, J. De La Torre Medina, M. Lemaitre, L. Piraux, Magnetic and magnetoresistive properties of 3d interconnected nico nanowire networks, Nanoscale Res. Lett. 11 (1) (2016a) 466.
[47] J. de la Torre Medina, T. da Câmara Santa Clara Gomes, Y.G. Velázquez Galván, L. Piraux, Large-scale 3-d interconnected ni nanotube networks with controlled structural and magnetic properties, Sci. Rep. 8 (1) (2018) 14555.
[48] E. Ferain, R. Legras, Track-etch templates designed for micro- and nanofabrication, Nucl. Instrum. Methods Phys. Res. Sect. B Beam Interact. Mater. Atoms 208 (2003) 115–122.
[49] N. Marchal, T. da Camara Santa Clara Gomes, F. Abreu Araujo, L. Piraux, Large spin-dependent thermoelectric effects in NiFe-based interconnected nanowire networks, Nanoscale Res. Lett. 15 (1) (2020) 137.
[50] T. da Câmara Santa Clara Gomes, N. Marchal, F. Abreu Araujo, L. Piraux, Tunable magnetoresistance and thermopower in interconnected NiCr and CoCr nanowire networks, Appl. Phys. Lett. 115 (24) (2019b) 242402.
[51] N. Marchal, T. da Câmara Santa Clara Gomes, F. Abreu Araujo, L. Piraux, Giant magnetoresistance and magneto-thermopower in 3d interconnected nixfel-x/cu multilayered nanowire networks, Nanomaterials 11 (2021) 1133.
[52] T. da Camara Santa Clara Gomes, N. Marchal, F. Abreu Araujo, Y. Velázquez Galván, J. de la Torre Medina, L. Piraux, Magneto-transport in flexible 3D networks made of interconnected magnetic nanowires and nanotubes, Nanomaterials 11 (1) (2021) 221.
[53] L. Piraux, J.M. George, J.F. Despres, C. Leroy, E. Ferain, R. Legras, K. Ounadjela, A. Fert, Giant magnetoresistance in magnetic multilayered nanowires, Appl. Phys. Lett. 65 (19) (1994) 2484–2486.
[54] A. Fert, L. Piraux, Magnetic nanowires, J. Magn. Magn Mater. 200 (1) (1999) 338–358.
[55] J.G. Hust, R.L. Powell, D.H. Weitzel, Thermal conductivity standard reference materials from 4 to 300 k. i. armco iron: including apparatus description and error analysis, J. Res. Natl. Bureau Stand., Sect. A, Phys. Chem. 74A (5) (1970) 673–690.
[56] M.J. Laubitz, T. Matsumura, P.J. Kelly, Transport properties of the ferromagnetic metals. ii. nickel, Can. J. Phys. 54 (1) (1976) 92–102.
[57] M.J. Laubitz, T. Matsumura, Transport properties of the ferromagnetic metals. i. cobalt, Can. J. Phys. 51 (12) (1973) 1247–1256.
[58] T. Farrell, D. Greig, The thermoelectric power of nickel and its alloys, J. Phys. C Solid State Phys. 3 (1) (1970) 138.
[59] M.C. Cadeville, J. Roussel, Thermoelectric power and electronic structure of dilute alloys of nickel and cobalt with d transition elements, J. Phys. F Met. Phys. 1 (5) (1971) 686.

[60] I. Campbell, A. Fert, Chapter 9 Transport Properties of Ferromagnets, Vol. 3 of Handbook of Ferromagnetic Materials, Elsevier, 1982.
[61] D.K.C. MacDonald, Thermoelectricity: An Introduction to the Principles, Wiley, 1962.
[62] S.F. Lee, W.P. Pratt, R. Loloee, P.A. Schroeder, J. Bass, "field-dependent interface resistance" of ag/co multilayers, Phys. Rev. B 46 (1992) 548–551.
[63] J. Bass, Cpp magnetoresistance of magnetic multilayers: a critical review, J. Magn. Magn Mater. 408 (2016) 244–320.
[64] J. Shi, S.S.P. Parkin, L. Xing, M.B. Salamon, Giant magnetoresistance and magneto-thermopower in co/cu multilayers, J. Magn. Magn Mater. 125 (3) (1993) L251–L256.